International Journal of Solids and Structures 47 (2010) 912–921

Contents lists available at ScienceDirect

International Journal of Solids and Structures

journal homepage: www.elsevier.com/locate/ijsolstr

An adhesive wear model of fractal surfaces in normal contact

X. Yin, K. Komvopoulos *

Department of Mechanical Engineering, University of California, Berkeley, CA 94720, USA

ARTICLE INFO

Article history:
Received 1 September 2009
Received in revised form 10 November 2009
Available online 11 December 2009

Keywords:
Adhesion
Asperity
Compatibility
Deformation
Fractal surfaces
Material properties
Roughness
Surface energy
Topography
Wear

ABSTRACT

A generalized adhesive wear analysis that takes into account the effect of interfacial adhesion on the total load was developed for three-dimensional fractal surfaces in normal contact. A wear criterion based on the critical contact area for fully-plastic deformation of the asperity contacts was used to model the removal of material from the contact interface. The fraction of fully-plastic asperity contacts, wear rate, and wear coefficient are expressed in terms of the total normal load (global interference), fractal (topography) parameters, elastic–plastic material properties, surface energy, material compatibility, and interfacial adhesion characteristics controlled by the environment of the interacting surfaces. Numerical results are presented for representative ceramic–ceramic, ceramic–metallic, and metal–metal contact systems to illustrate the dependence of asperity plastic deformation, wear rate, and wear coefficient on global interference, surface roughness, material properties, and work of adhesion (affected by the material compatibility and the environment of the contacting surfaces). The analysis yields insight into the effects of surface material properties and interfacial adhesion on the adhesive wear of rough surfaces in normal contact.

1. Introduction

Wear plays an important role in many fields of science and technology. The implications of wear can be either beneficial or detrimental to the performance of scientific instruments and engineering components possessing contact interfaces. Since the seminal study of adhesive wear by Archard (1953), several wear mechanisms have been proposed to explain the loss of material from sliding surfaces, including abrasion, corrosion, erosion, contact fatigue, and delamination (Kruschov, 1957; Suh, 1973, 1986). Among various wear mechanisms, adhesive wear is the most common process of material removal encountered over a wide range of length scales. This type of wear is responsible for the failure of many mechanical and electromechanical components whose functionality depends on the tribological properties of contact interfaces. Thus, accurate prediction of the adhesive wear rate in tribological systems is of great technological and scientific importance.

Significant research effort has been devoted to study the dependence of adhesive wear on various factors, such as normal load, sliding speed, interfacial adhesion/friction conditions, and material properties (Lisowski and Stolarski, 1981; Finkin, 1972; Paretkar et al., 1996; Yang, 2003). Archard's wear model has been used extensively to quantify the wear rate of sliding surfaces (Qureshi and Sheikh, 1997; Yang, 2004), develop adhesion models of single-asperity junctions (Rabinowicz, 1980), and perform energy-based analyses of adhering asperities (Warren and Wert, 1990). However, the majority of relationships between adhesive wear rate, sliding speed, and contact area reported in early studies were based on semi-empirical approaches and statistical topography parameters (e.g., mean and variance of the surface heights, slopes, and curvatures) that do not account for the scale dependence of topography parameters, a characteristic feature of multi-scale roughness of engineering surfaces.

To overcome shortcomings with scale-dependent statistical surface parameters (Greenwood and Williamson, 1966) and random process theory (Nayak, 1973) commonly used in contact mechanics, the surface topography in contemporary contact analyses was described by fractal geometry (Majumdar and Bhushan, 1990, 1991; Wang and Komvopoulos, 1994a,b, 1995; Sahoo and Roy Chowdhury, 1996; Komvopoulos and Yan, 1998; Borri-Brunetto et al., 1999; Ciavarella et al., 2000; Komvopoulos and Ye, 2001; Persson et al., 2002; Yang and Komvopoulos, 2005; Gong and Komvopoulos, 2005a,b; Komvopoulos and Yang, 2006; Komvopoulos and Gong, 2007; Komvopoulos, 2008). Because fractal geometry is characterized by the properties of continuity, non-differentiability, scale invariance, and self-affinity (Mandelbrot, 1983), it has been used in various fields of science and engineering to describe disordered phenomena, including changes in surface topography due to wear and fracture processes. For example, Zhou et al. (1993) used a fractal contact model to examine the

* Corresponding author. Tel.: +1 510 642 2563; fax: +1 510 643 5599.
E-mail address: kyriakos@me.berkeley.edu (K. Komvopoulos).

0020-7683/$ - see front matter © 2009 Elsevier Ltd. All rights reserved.
doi:10.1016/j.ijsolstr.2009.12.003

Nomenclature

a'	truncated contact area or large-base area of spherical segment
a'_C	critical truncated contact area
a'_L	largest truncated contact area
a'_{Li}, a'_{Lk}	largest truncated contact area at the ith and kth increment of global interference
a'_S	smallest truncated contact area
c_l	lubrication compatibility index
c_m	metallurgical compatibility index
dh	increment of global interference or height of spherical segment
dV_p^i, dV_p^k	wear volume at the ith and kth increment of global interference
$dV_{e,1}$	volume of an elastic asperity approximated by a spherical cap
$dV_{p,1}$	volume of a fully-plastic asperity approximated by a spherical segment
D	fractal dimension
E^*	effective elastic modulus
E_i	elastic modulus of surface i (i = A, B)
F_e	total normal force due to elastic asperity contacts
F_p	total normal force due to fully-plastic asperity contacts
F	total normal force
G	fractal roughness
h	global interference
H^*	effective hardness
H_i	hardness of surface i (i = A, B)
K	adhesive wear coefficient
L	sample length
L_S	smallest characteristic (cut-off) length
m	ridge index
M	number of superposed ridges
n	asperity contact size distribution
N	number of asperity contacts with truncated areas greater than a specific truncated contact area
p_m	mean contact pressure
q	spatial frequency index
q_{max}	maximum value of spatial index
r	real contact radius of an asperity contact
r'	radius of a truncated asperity contact or base radius of spherical cap
r'_S	radius of smallest truncated asperity contact
R	equivalent radius of curvature of spherical asperity
S'	total truncated contact area
S'_e	total truncated contact area of elastic asperity contacts
S'_p	total truncated contact area of fully-plastic asperity contacts
S_a	apparent sample area
V	total wear volume
V_e	total volume of elastic asperities
V_p	total volume of fully-plastic asperities
V_t	total volume of contacting asperities
W_{AB}	work of adhesion of contacting surfaces A and B
x,y	in-plane Cartesian coordinates
z	out-of-plane Cartesian coordinate or surface height function
z_0	equilibrium separation distance of two surfaces

Greek symbols

γ	profile frequency density control parameter
Γ_i	surface energy of surface i (i = A, B)
δ	local interference, height of a spherical cap, or distance between large base and top of spherical cap at the lower end of a spherical segment
δ_{min}	minimum local interference
ΔF_e	normal force at an elastic asperity contact
ΔF_p	normal force at a fully-plastic asperity contact
μ	Tabor parameter
ν_i	Poisson's ratio of surface i (i = A, B)
σ	rms roughness of equivalent surface
σ_Y	effective yield strength
$\phi_{m,q}$	random phase generator
ω	spatial frequency of surface profile
ω_h	highest frequency of surface profile
ω_l	lowest frequency of surface profile

dependence of the adhesive wear rate on fractal parameters and material properties, Shirong and Gouan (1999) developed a fractal model of adhesive wear for the running-in stage of sliding, and Sahoo and Roy Chowdhury (2002) studied the effect of adhesion between contacting asperities on the adhesive wear behavior of fractal surfaces subjected to light loads. Although the previous studies have provided insight into the effects of fractal dimension, material properties, and surface adhesion on the loss of material by adhesive wear, the developed wear models are extensions of Archard's model and, therefore, can only be applied to sliding surfaces. However, experimental evidence (Martin et al., 2002) and molecular dynamics simulations (Bhushan et al., 1995) have shown that adhesive wear can occur even in the absence of relative slip between the contacting surfaces. Hence, a comprehensive adhesive wear theory of rough surfaces in normal contact is necessary to bridge this gap of knowledge.

The main objective of the present analysis is twofold. First, instead of an empirical approach based on experimental results and observed trends, an adhesive wear model of rough surfaces in normal contact is derived based on plasticity-induced wear behavior that accounts for adhesion between interacting asperities. Second, the adhesive wear rate and wear coefficient are obtained in terms of the total normal load (global interference), surface topography (fractal) parameters, elastic–plastic material properties, and interfacial adhesion characteristics that depend on the material compatibility and contact environment. Results for representative contact systems with fractal surface topographies reveal the effects of roughness, surface material properties, and interfacial adhesion on adhesive wear.

2. Surface description

Normal contact of two rough surfaces can be analyzed by an equivalent contact model consisting of a deformable rough surface with effective material properties and equivalent roughness in contact with a rigid plane (Greenwood and Williamson, 1966). The effective elastic modulus E^* and hardness H^* of the equivalent surface are given by

$$\frac{1}{E^*} = \frac{1-\nu_A^2}{E_A} + \frac{1-\nu_B^2}{E_B} \tag{1}$$

$$H^* = \min[H_A, H_B] \tag{2}$$

where subscripts A and B refer to the two surfaces in normal contact, and E, ν, and H denote elastic modulus, Poisson's ratio, and hardness, respectively.

In the present analysis, the equivalent rough (fractal) surface is assumed to be isotropic and self-affine, and its three-dimensional (3D) surface profile $z(x,y)$ is given by (Yan and Komvopoulos, 1998)

$$z(x,y) = L\left(\frac{G}{L}\right)^{(D-2)}\left(\frac{\ln\gamma}{M}\right)^{1/2}\sum_{m=1}^{M}\sum_{q=0}^{q_{\max}}\gamma^{(D-3)q} \times\left\{\cos\phi_{m,q} - \cos\left[\frac{2\pi\gamma^q(x^2+y^2)^{1/2}}{L} \times\cos\left(\tan^{-1}\left(\frac{y}{x}\right) - \frac{\pi m}{M}\right) + \phi_{m,q}\right]\right\} \quad (3)$$

where D ($2 < D < 3$) and G are the fractal dimension and fractal roughness, respectively, both independent of wavelength in the range where the surface exhibits fractal behavior, L is the sample length, M is the number of superimposed ridges, $\phi_{m,q}$ is a random phase uniformly distributed in the range $[0,2\pi]$ by a random number generator to prevent the coincidence of different frequencies at any point of the surface profile, q is a spatial frequency index, and γ ($\gamma > 1$) controls the density of frequencies in the surface profile. Surface flatness and frequency distribution density considerations suggest that $\gamma = 1.5$ is typical for most surfaces (Komvopoulos and Yan, 1997).

The fractal parameter D determines the relative contributions of high- and low-frequency components in the surface profile. The amplitudes of high-frequency components become comparable to those of low-frequency components with increasing D, whereas the amplitudes of wavelengths comprising the surface profile intensify with increasing G. Because of the scale invariance of D and G, fractal surface description at different length scales is independent of measurement scale. The shortest wavelength corresponds to the instrument resolution limit and the longest wavelength is equal to the sample length. For a continuum description to hold, the shortest wavelength is set above a cut-off length L_S, typically on the order of the material's interatomic distance. Thus, the highest and lowest frequencies in the surface profile are $\omega_h = 1/L_S$ and $\omega_l = 1/L$, respectively. The lower limit of q is zero, while its upper limit is given by $q_{\max} = \text{int}[\log(L/L_S)/\log\gamma]$.

A surface profile generated from Eq. (3) exhibits scale invariance in a finite range of length scale, outside of which the surface topography can be characterized by a deterministic function (Wang and Komvopoulos, 1994b). A typical 3D fractal surface constructed from Eq. (3) is shown in Fig. 1. Eq. (3) was used to generate the 3D rough (fractal) surfaces used in the elastic–plastic contact analysis presented in the following section.

3. Contact mechanics analysis

Because the equivalent rough surface is assumed to be isotropic, any two-dimensional (2D) surface profile is a statistical representation of the 3D surface topography. Fig. 2 shows a 2D profile of a rough surface truncated by a rigid plane. The advancement of the rigid plane toward the rough surface by interference increments dh leads to the formation of truncated segments. Each truncated segment is approximated by an asperity with a spherical cap shape having a base radius r' equal to one-fourth of the asperity's base wavelength and height equal to the local interference δ given by (Yan and Komvopoulos, 1998)

$$\delta = 2G^{(D-2)}(\ln\gamma)^{1/2}(2r')^{(3-D)} \quad (4)$$

The size distribution function of asperity contacts is a fundamental concept in contact mechanics. Asperity contacts resulting from the truncation of a rough surface by a rigid plane follow an island distribution similar to that observed in geophysics (Mandelbrot, 1975, 1983). This island-like distribution was used in earlier contact mechanics studies of fractal surfaces (Majumdar and Bhushan, 1991; Wang and Komvopoulos, 1994a,b, 1995; Komvopoulos and Yan, 1997; Yan and Komvopoulos, 1998; Komvopoulos and Ye, 2001) and also the present analysis. This island distribution obeys the following power-law relationship:

$$N(a') = \left(\frac{a'_L}{a'}\right)^{(D-1)/2} \quad (5)$$

where $N(a')$ is the number of asperities with truncated areas larger than a', and a'_L is the largest truncated contact area at a given global interference h. The contact size distribution of the truncated asperities $n(a')$ of a 3D surface profile is given by (Yan and Komvopoulos, 1998)

$$n(a') = -\frac{dN(a')}{da'} = \frac{(D-1)}{2a'_L}\left(\frac{a'_L}{a'}\right)^{(D+1)/2} \quad (6)$$

Thus the number of truncated asperities with areas between a' and $a' + da'$ is equal to $n(a')da'$.

At a given global interference, a'_L can be determined from the total truncated area S' of the equivalent rough surface using the relationship (Komvopoulos and Ye, 2001):

$$S' = \int_{a'_S}^{a'_L} a'n(a')\,da' \quad (7)$$

where a'_S is the smallest truncated contact area, which for a continuum description to hold must be greater than the atomic dimensions. For example, the diameter of the smallest truncated contact

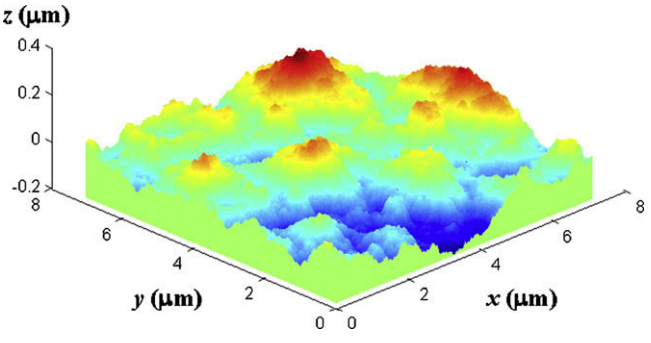

Fig. 1. Three-dimensional fractal surface generated from Eq. (3) for $D = 2.24$, $G = 2.39 \times 10^{-4}$ nm, $M = 10$, $\gamma = 1.5$, $L = 7.04 \times 10^3$ nm, and $L_S = 5$ nm ($\sigma = 290$ nm).

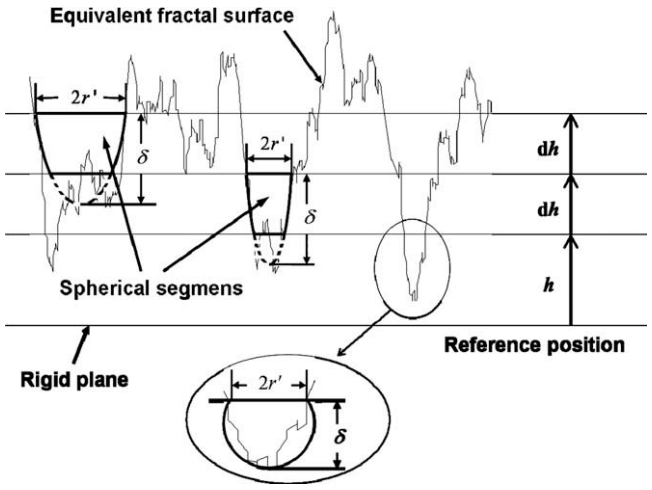

Fig. 2. Two-dimensional profile of a rough (fractal) surface truncated by a rigid plane.

asperity can be set equal to ~5–6 times the lattice parameter of the softer material.

After substituting Eq. (6) into Eq. (7) and integrating, the total truncated area can be expressed as

$$S' = \left(\frac{D-1}{3-D}\right) a'_L \left[1 - \left(\frac{a'_S}{a'_L}\right)^{(3-D)/2}\right] \tag{8}$$

The total truncated area at a given global interference was obtained numerically by summing up the contact areas of all truncated asperities on the equivalent rough surface (Komvopoulos and Ye, 2001). Then, a'_L was determined from Eq. (8) in terms of a'_S, D, and S'. Finally, Eqs. (6) and (8) were used to obtain the area range $[a'_S, a'_L]$ and, in turn, the spatial distribution of the truncated asperity contacts at a given global interference.

Before proceeding with the adhesive wear analysis of rough surfaces in normal contact it is necessary to consider surface deformation at the asperity level. Yan and Komvopoulos (1998) derived a relationship of the critical truncated contact area at the transition from elastic to fully-plastic asperity deformation, whereas Wang and Komvopoulos (1994b) included in their analysis the intermediate regime of elastic–plastic deformation and derived relationships for the critical truncated contact area for elastic–plastic and fully-plastic asperity deformation. In the present study, asperity deformation is assumed to follow an elastic–perfectly plastic material behavior, implying either elastic or fully-plastic deformation at asperity contacts, depending on the local surface interference and truncated asperity contact area. Because wear implies the removal of material as a consequence of irreversible deformation, it is assumed that only fully-plastic asperity contacts contribute to material removal. The effect of neglecting the intermediate regime of elastic–plastic deformation included in previous contact mechanics studies (Komvopoulos and Ye, 2001; Kogut and Etsion, 2002; Kogut and Komvopoulos, 2004; Mukherjee et al., 2004; Komvopoulos, 2008) in the present analysis of adhesive wear can be interpreted in the context of Fig. 3. Since wear particles are not likely to form from asperities in the lower range of elastic–plastic deformation, the elastic–fully plastic behavior is a reasonable approximation that also results in significant enhancement of the computational efficiency.

Fully-plastic deformation of an asperity contact occurs when $a' \leqslant a'_C$, whereas elastic deformation arises when $a' > a'_C$, where

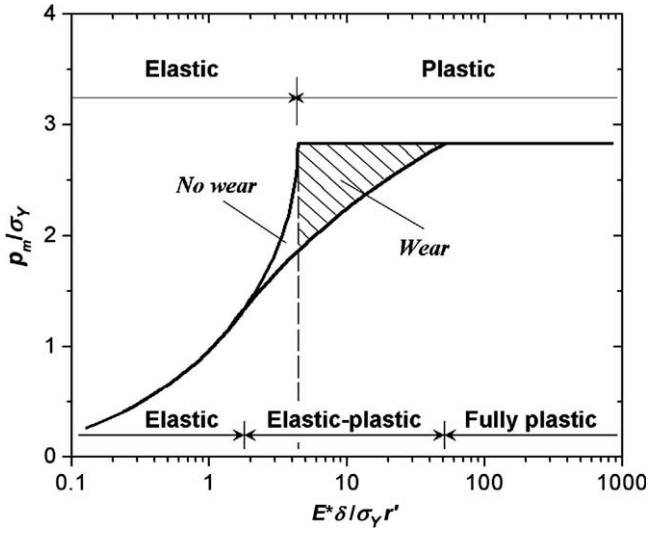

Fig. 3. Normalized mean contact pressure p_m/σ_Y versus normalized representative strain $E^*\delta/\sigma_Y r'$ for two constitutive models of asperity deformation.

a'_C is the critical truncated contact area for fully-plastic deformation, obtained from the classical definition of material hardness,

$$H^* = \frac{\Delta F_e|_{a'=a'_C}}{a'_C} \tag{9}$$

where ΔF_e is the normal load at an elastic asperity contact calculated for $a' = a'_C$. The equation of the normal load derived from Hertz theory, modified to include the effect of interfacial adhesion (Johnson et al., 1971), is given by

$$\Delta F_e = \frac{4E^* r^3}{3R} - \left[8\pi W_{AB} E^* r^3\right]^{1/2} \tag{10}$$

where r is the contact radius of an elastically deformed spherical asperity, related to the truncated contact area by

$$r = \left[\frac{a'}{2\pi}\right]^{1/2}, \tag{11}$$

R is the asperity radius of curvature given by (Yan and Komvopoulos, 1998)

$$R = \frac{(a')^{(D-1)/2}}{2^{(5-D)}\pi^{(D-1)/2} G^{(D-2)} (\ln\gamma)^{1/2}}, \tag{12}$$

and W_{AB} is the work of adhesion of contacting surfaces A and B, expressed as (Rabinowicz, 1977)

$$W_{AB} = c_m c_l (\Gamma_A + \Gamma_B) \tag{13}$$

where c_m is the material compatibility index (controlled by the solid solubility limit of materials A and B), c_l is the lubrication compatibility index, which depends on the environment of the interacting surfaces, and Γ_A and Γ_B are the surface energies of materials A and B, respectively.

Fig. 4 shows schematically the truncation and deformation of an asperity by a rigid plane. Eqs. (9)–(13) indicate that a'_C is a function of effective material properties E^* and H^*, fractal parameters of the equivalent rough surface D and G, surface energies Γ_A and Γ_B, and interfacial adhesion controlled by the magnitude of the composite compatibility index $c_m c_l$.

When $a'_L > a'_C$, elastic and fully-plastic asperity contacts co-exist at the interface. The total truncated contact area of elastic and fully-plastic asperity contacts, S'_e and S'_p, respectively, can be written as

$$S'_e = \int_{a'_C}^{a'_L} a' n(a')\, da' \tag{14}$$

$$S'_p = \int_{a'_S}^{a'_C} a' n(a')\, da' \tag{15}$$

After substituting Eq. (6) into Eqs. (14) and (15) and integrating,

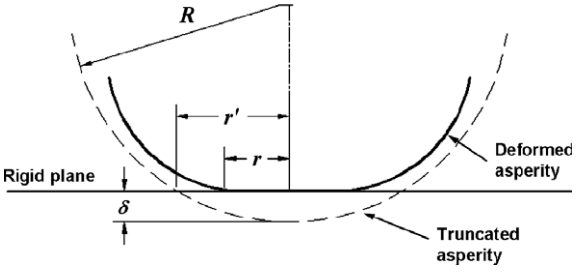

Fig. 4. Schematics of truncation and deformation of an asperity by a rigid plane.

$$S'_e = \left(\frac{D-1}{3-D}\right) a'_L \left[1 - \left(\frac{a'_C}{a'_L}\right)^{(3-D)/2}\right] \tag{16}$$

$$S'_p = \left(\frac{D-1}{3-D}\right) a'_L{}^{(D-1)/2} \left(a'_C{}^{(3-D)/2} - a'_S{}^{(3-D)/2}\right) \tag{17}$$

Hence, the total truncated contact area S' can be expressed as

$$S' = S'_e + S'_p = \left(\frac{D-1}{3-D}\right) a'_L \left[1 - \left(\frac{a'_S}{a'_L}\right)^{(3-D)/2}\right] \tag{18}$$

For relatively small global interference (light load), the average spacing of asperity contacts is much larger than the asperity contact sizes. Also, only the largest wavelength in the waveform of a truncated asperity is considered in the analysis, i.e., all the smaller asperities residing on the largest asperity are neglected. Based on these two facts, the effect of asperity interaction (Sahoo and Banerjee, 2005; Sahoo, 2006) was ignored in the present analysis as secondary.

The total normal load F can be obtained as the sum of the total forces of elastic and fully-plastic asperity contacts, F_e and F_p, respectively, i.e.,

$$F = F_e + F_p \tag{19}$$

$$F_e = \int_{a'_C}^{a'_L} \Delta F_e(a') n(a')\, da' \tag{20}$$

$$F_p = \int_{a'_S}^{a'_C} \Delta F_p(a') n(a')\, da' \tag{21}$$

where ΔF_e is given by Eq. (10) and ΔF_p is the normal load at a fully-plastic asperity contact given by (Roy Chowdhury and Pollock, 1981)

$$\Delta F_p = a' H^* - 2\pi W_{AB} R \tag{22}$$

Eqs. (6), (9)–(13) and (19)–(22) indicate that the total normal load is a function of the elastic–plastic material properties, the topography of the equivalent rough (fractal) surface, the interfacial adhesion (controlled by the material compatibility and contact environment), and the largest and smallest contact areas of truncated asperities.

The wear volume at a given global interference h was calculated by the following numerical procedure. At each increment of global interference dh, the volumes of spherical segments used to approximate fully-plastic asperity contacts were subtracted from the surface profile, as illustrated schematically in Fig. 2. The incremental truncation of the surface profile by the rigid plane resulted in the cumulative removal of material from fully-plastic asperity contacts. Wear particles of uniform shape (i.e., spherical segments) were produced from all fully-plastic asperity contacts by setting the interference increment dh equal to the minimum local interference δ_{min} (Yan and Komvopoulos, 1998), i.e.,

$$dh = \delta_{min} = 2G^{(D-2)} (\ln \gamma)^{1/2} (2r'_S)^{(3-D)} \tag{23}$$

where r'_S is the truncated radius of the smallest asperity contact. The removed spherical segment has a sphere radius R, large-base area a', large-to-small base distance dh, and distance between the large base and the apex of the spherical cap at the bottom of the spherical segment equal to δ (Fig. 2). Thus, the volume of a wear particle approximated by a spherical segment $dV_{p,1}$ can be written as

$$dV_{p,1} = \left(\frac{a' - \pi\delta^2}{2} + \pi R\delta\right) dh - \pi(R-\delta) dh^2 - \frac{\pi}{3} dh^3 \tag{24}$$

Surface contact at a given global interference and corresponding adhesive wear were assumed to be time-independent processes, i.e., the present analysis is applicable to materials exhibiting time-independent deformation and static loads. The incremental interference scheme described previously was only used to enhance the calculation accuracy of the total wear volume at a given global interference (by capturing the details of the surface profile at small interference increments) and does not imply wear accumulation due to repeated contact under different loads.

The wear rate at a given global interference is defined as the ratio of the total wear volume dV_p^k calculated in the last (kth) interference increment dh ($=h/k$) to the global interference increment dh, where dV_p^k is the sum of the volumes of all wear particles removed from the rough surface at the kth interference increment. Hence,

$$dV_p^k = \int_{a'_S}^{a'_C} dV_{p,1}(a') n(a', a'_{Lk})\, da' \tag{25}$$

where a'_{Lk} is the largest truncated contact area at the kth interference increment.

The wear coefficient K is defined as the total volume of wear particles V divided by the total volume of all contacting asperities V_t, i.e.,

$$K = \frac{V}{V_t} = \frac{V_p}{V_p + V_e} \tag{26}$$

where V_e and V_p are the total volumes of elastic and fully-plastic asperity contacts, respectively. The cumulated total wear volume V_p is given by

$$V_p = \sum_{i=1}^{k} dV_p^i \tag{27}$$

where dV_p^i is the wear volume at the ith increment, obtained as the sum of the volumes of all wear particles generated at this increment, i.e.,

$$dV_p^i = \int_{a'_S}^{a'_C} dV_{p,1}(a') n(a', a'_{Li})\, da' \tag{28}$$

where a'_{Li} is the largest truncated contact area at the ith increment.

The total volume of elastically deformed asperity contacts at a given global interference (obtained in one numerical step) is

$$V_e = \int_{a'_C}^{a'_{Lk}} dV_{e,1}(a') n(a', a'_{Lk})\, da' \tag{29}$$

where $dV_{e,1}$ is the volume of an elastic asperity contact approximated by a spherical cap of base area a' and height δ given by

$$dV_{e,1} = \frac{1}{2} a'\delta + \frac{\pi}{6}\delta^3 \tag{30}$$

Eqs. (4), (6), (8)–(13) and (23)–(30) indicate that both the wear rate dV_p^k/dh and the wear coefficient K depend on the elastic–plastic material properties, topography (fractal) parameters, surface energies, material compatibility, interfacial adhesion, and (indirectly) total normal load through the total truncated contact area S' that controls the magnitude of a'_L (Eq. (8)).

4. Numerical results and discussion

A contact mechanics analysis of adhesive wear of rough surfaces exhibiting fractal behavior was presented in the previous sections. Because it is impossible to obtain a closed-form solution for the critical truncated contact area a'_C to determine the deformation mode at each asperity contact and then calculate the wear rate and wear coefficient, numerical results are presented in this section for typical material properties and different interfacial adhesion conditions and surface roughness. The contact systems selected for numerical analysis, associated material properties, and corresponding composite compatibility index are given in Tables 1 and 2, respectively. These contact systems are representative of

Table 1
Properties of contact surfaces.

Contact system	Material	Properties[a]					
		Γ (mN/m)	E (GPa)	v	H (GPa)	E^* (GPa)	H^* (GPa)
Al_2O_3/TiC	Al_2O_3	740	307	0.25	27.6	192	23.5
	TiC	900	450	0.18	23.5		
Al_2O_3/CrN	Al_2O_3	740	307	0.25	27.6	84.0	14.8
	CrN	44.3	103	0.30	14.8		
AISI 1095/AISI 1020	AISI 1095	1700	200	0.29	6.08	109	1.71
	AISI 1020	1700	200	0.29	1.71		

[a] Sources: Suh (1986) and Komvopoulos and Zhang (2008).

Table 2
Composite compatibility index of contact surfaces at different environments.

Contact system	Combined compatibility index, $c_m c_l$[a]				
	Vacuum	Clean air	Poor lubricant	Fair lubricant	Good lubricant
Al_2O_3/TiC	0.40	0.36	0.27	0.20	0.15
Al_2O_3/CrN	0.40	0.36	0.27	0.20	0.15
AISI 1095/AISI 1020	1.50	1.00	0.37	0.14	0.05

[a] Source: Rabinowicz (1977).

ceramic–ceramic (Al_2O_3/TiC), ceramic–metallic (Al_2O_3/CrN), and metal–metal (AISI 1095/AISI 1020) contact interfaces. The numerical results presented in this section are for a 3D equivalent surface topography generated from Eq. (3) for $\gamma = 1.5$, $M = 10$, $L_S = 5$ nm, $L = 7.04 \times 10^3$ nm, and $\phi_{m,q} = \pi/2$. In all cases, a'_S was scaled to the smallest wavelength existing in the surface profile, i.e., $a'_S = \pi(r'_S)^2 = \pi(L_S/2)^2 = 19.6\ \text{nm}^2$. Unless otherwise stated, the fractal parameters of the 3D equivalent surface topography are D = 2.24 and $G = 2.39 \times 10^{-4}$ nm ($\sigma = 290$ nm). The effects of material properties, interfacial adhesion (i.e., effects of material compatibility and environment), and surface topography (i.e., roughness effect) on the deformation mode of asperity contacts are discussed first, followed by the presentation of wear rate and wear coefficient results and a discussion of the applicability of the present analysis.

4.1. Deformation mode of asperity contacts

The effect of the work of adhesion, controlled by the surface energies of the interacting surfaces (Table 1) and the combined compatibility index $c_m c_l$ (Table 2), on the deformation mode of the asperity contacts can be interpreted in terms of the dependence of a'_C (Eq. (9)) on contact environment shown in Fig. 5. The trend is for a'_C to decrease with the work of adhesion (or interfacial adhesion) resulting from the enhancement of the lubrication efficacy. The highest a'_C corresponds to the metal–metal contact system in vacuum, and the lowest a'_C to the ceramic–metallic system at any environment. The results shown in Fig. 5 reveal a strong effect of interfacial adhesion (effects of material compatibility and contact environment) and elastic–plastic material properties on the dominance of plasticity at the contact interface.

Fig. 6 shows the effect of surface roughness σ on the deformation mode of asperity contacts under vacuum conditions, i.e., highest $c_m c_l$ value for each contact system (Table 2). The equivalent surface roughness σ was varied in the range of 1–10^4 nm by varying the fractal roughness G between 1.94×10^{-14} and 4.88×10^2 nm and fixing the fractal dimension ($D = 2.24$). Surface topographies with $\sigma = 1$ and 10^4 nm are typical of ultra-smooth surfaces (e.g., wafers) and well-polished bearing surfaces, respectively. In all cases, a'_C tends to increase monotonically with surface roughness. The results show a strong dependence of a'_C on both

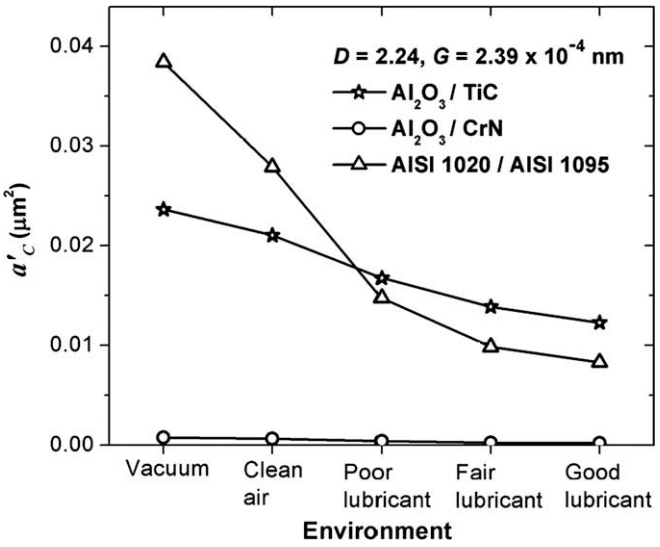

Fig. 5. Critical truncated contact area a'_C versus environment (interfacial adhesion) for surface properties given in Tables 1 and 2 ($\sigma = 290$ nm).

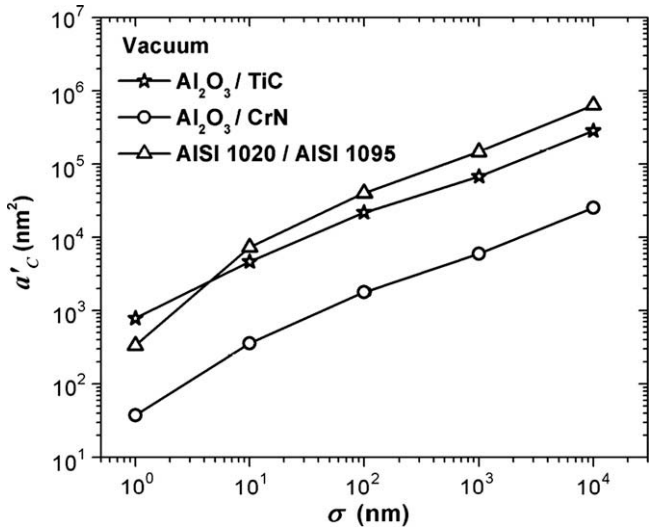

Fig. 6. Critical truncated contact area a'_C versus rms roughness of equivalent surface σ ($D = 2.24$) for surface properties given in Tables 1 and 2.

material properties and surface roughness. For example, a'_C of the metal–metal contact system is less than that of the ceramic–ceramic contact system in the case of ultra-smooth surfaces

($\sigma = 1$ nm), whereas the opposite is observed for relatively rough surfaces ($\sigma > 10$ nm).

To examine the evolution of plasticity at the contact interface in terms of the global interference (normal load), the total truncated contact area of fully-plastic asperity contacts S'_p normalized by the apparent sample area S_a ($S_a = L^2$) is shown in Fig. 7 as a function of global interference h for fixed surface topography and environment (vacuum). In all cases, $S'_p/S_a \ll 1$ (despite the wide variation of the global interference) and S'_p increases linearly with global interference. This trend can be explained by considering that both a'_L and S'_p increase with S' (Eqs. (8) and (17), respectively) and that S' increases with h. For a given global interference, Fig. 7 shows that S'_p/S_a is a strong function of material properties, in accord with Eq. (17) and the results shown in Fig. 5 for vacuum.

The ratio of the total truncated contact area of fully-plastic asperities to the total truncated contact area S'_p/S', shown in Fig. 8 as a function of global interference h for fixed topography ($\sigma = 290$ nm) and environment (vacuum), can be used to further examine the dominant deformation mode at the asperity level. The low-order of magnitude of S'_p/S' indicates that fully-plastic asperities represent a small percentage of all the asperity contacts comprising the total truncated contact area, implying the dominance of elastic deformation at the asperity level. Eqs. (17) and (18) and Fig. 5 indicate that, for fixed global interference, topography parameters (roughness), and contact environment, S'_p/S' depends on a'_C. The rapid decrease in S'_p/S' with increasing h in the low-interference range ($h < \sim 70$ nm) reveals an enhancement of the dominance of elastic deformation at the asperity level with increasing global interference. This trend can be attributed to the decreasing trend of S'_p/S' with increasing a'_L (or global interference), deduced from Eqs. (17) and (18). The small negative slope of S'_p/S' in the upper-interference range ($h > \sim 70$ nm) implies that the variation of the global interference within this range does not affect significantly the relative contribution of plastic deformation to the overall deformation at the contact interface. The critical global interference (~ 70 nm) demarcating the low-interference range from the upper-interference range is equal to $\sim 0.25\sigma$.

4.2. Wear rate

Fig. 9 shows the wear rate dV^k_p/dh as a function of global interference h of the three contact systems in vacuum. The linear increase in wear rate is a consequence of the increase in a'_L with global interference (Eq. (8)), which, for given a'_S and a'_C, yields a denser asperity distribution $n(a')$ (Eq. (6)), implying a higher wear volume dV^k_p (Eq. (25)). Fig. 9 shows that, for fixed topography parameters, global interference (i.e., fixed a'_L), and work of adhesion, dV^k_p/dh depends on the material properties, which control the magnitude of a'_C (Eq. (25)).

The effect of the work of adhesion (i.e., material compatibility and/or contact environment) on dV^k_p/dh for a given surface topography and fixed global interference can be interpreted in the context of the results shown in Fig. 10. The trend for dV^k_p/dh to decrease with the work of adhesion (or interfacial adhesion) due to the improvement of lubrication is similar to that shown in Fig. 5, and can be attributed to the dependence of dV^k_p/dh only on a'_C (Eq. (25)) for fixed topography and global interference. The lowest wear rate corresponds to the ceramic–metallic system (Al_2O_3/CrN), i.e., the contact system with the lowest work of adhesion at any environment.

The dependence of the wear rate dV^k_p/dh on the rms roughness of the equivalent surface σ (or fractal roughness G since $D = 2.24$) is shown in Fig. 11 for fixed global interference and environment

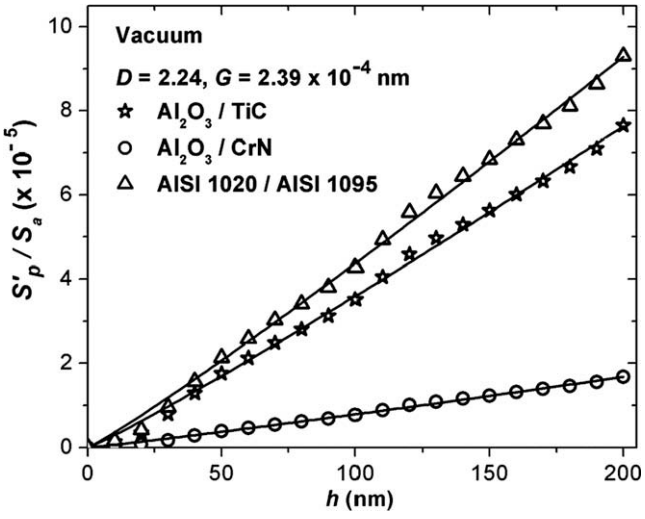

Fig. 7. Ratio of total truncated contact area of fully-plastic asperity contacts to apparent sample area S'_p/S_a versus global interference h for surface properties given in Tables 1 and 2 ($\sigma = 290$ nm).

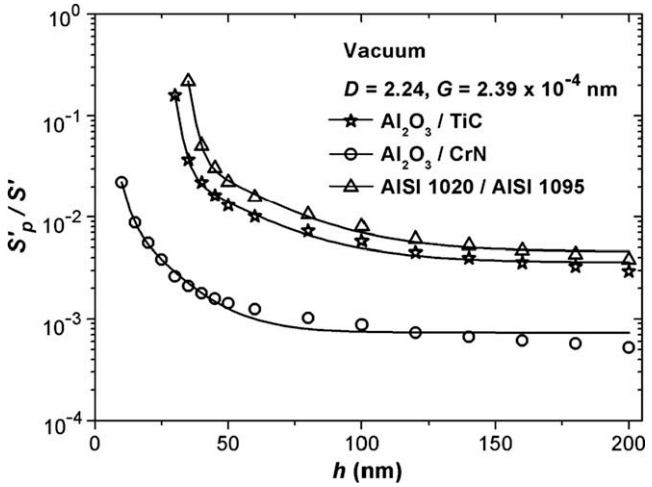

Fig. 8. Ratio of total truncated contact area of fully-plastic asperity contacts to total truncated contact area S'_p/S' versus global interference h for surface properties given in Tables 1 and 2 ($\sigma = 290$ nm).

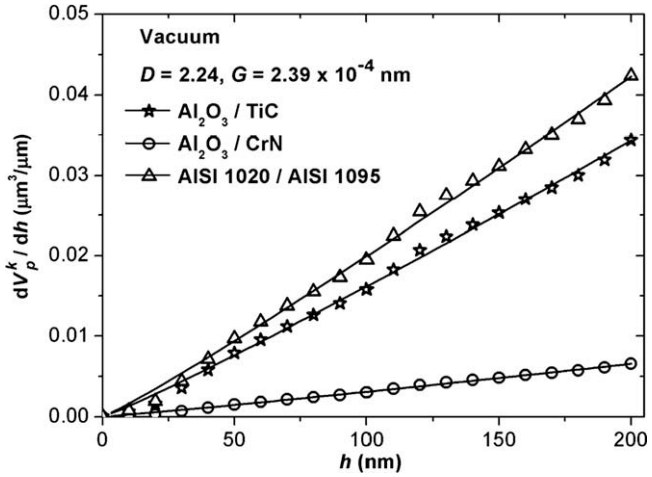

Fig. 9. Wear rate dV^k_p/dh versus global interference h for surface properties given in Tables 1 and 2 ($\sigma = 290$ nm).

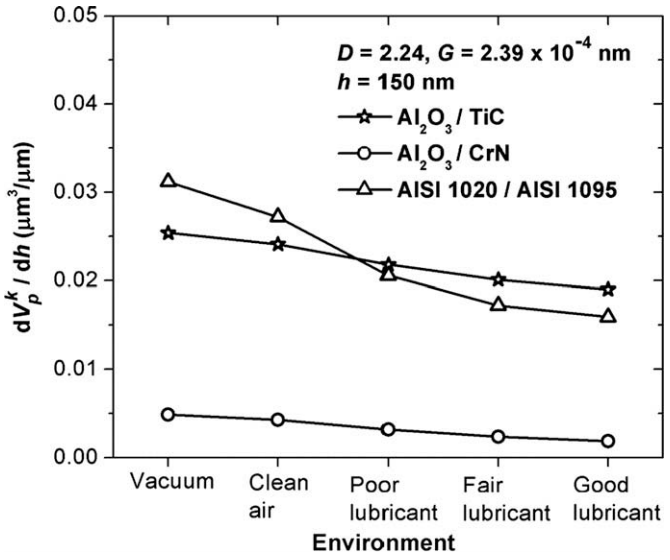

Fig. 10. Wear rate dV_p^k/dh versus environment (interfacial adhesion) for surface properties given in Tables 1 and 2 ($\sigma = 290$ nm).

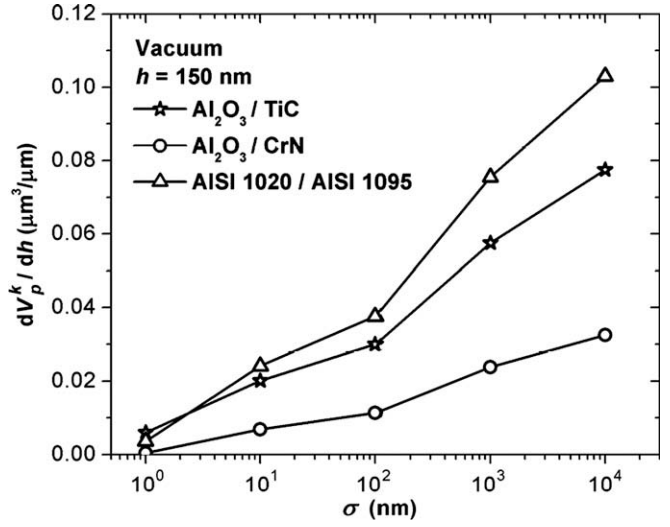

Fig. 11. Wear rate dV_p^k/dh versus rms roughness of equivalent surface σ ($D = 2.24$) for surface properties given in Tables 1 and 2.

(vacuum). The well-known trend of the wear rate to increase with surface roughness shown by all contact systems suggests that higher G values promote plastic deformation at the asperity level, thus enhancing the wear rate. This finding can be explained by considering the dependence of a'_C and a'_{Lk} on the equivalent surface roughness σ. The trend in Fig. 11 is similar to that shown in Fig. 6 (a'_C increases with σ) because, for fixed global interference and environment, dV_p^k/dh depends mainly on a'_C (Eq. (25)). Although the increase in G (or σ) decreases S', which, in turn, results in the decrease of both a'_{Lk} and $n(a')$ for fixed D and h (Eqs. (8) and (6), respectively), this effect is secondary (Eq. (25)) compared to that of a'_C. Thus, dV_p^k is mostly affected by the magnitude of a'_C.

4.3. Wear coefficient

Fig. 12 shows the wear coefficient K as a function of global interference h for fixed topography and environment (vacuum). In all cases, the wear coefficient is on the order of 10^{-4}, which is typical of adhesive wear of clean surfaces (Rabinowicz, 1995), and decreases rapidly with the increase of the global interference (normal load), reaching a steady state at a critical global interference that depends on the elastic–plastic material properties. The relatively high order of magnitude of K is typical of contacting surfaces in vacuum. As explained previously, for fixed global interference, topography (fractal parameters/roughness), and environment, S'_p/S' is controlled by a'_C, implying a dependence of plastic deformation and, in turn, wear coefficient on a'_C, as deduced from Eqs. (26)–(29). Indeed, the trend observed in Fig. 12 is similar to that seen in Fig. 8.

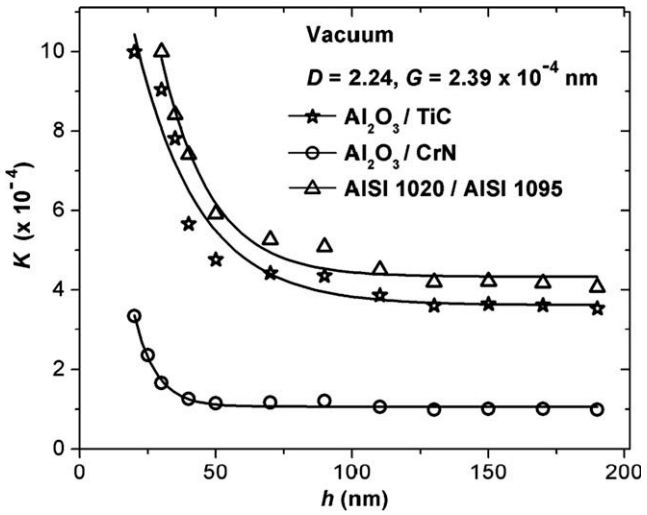

Fig. 12. Wear coefficient K versus global interference h for surface properties given in Tables 1 and 2 ($\sigma = 290$ nm).

The effect of the work of adhesion (contact environment) on the wear coefficient can be interpreted in light of Fig. 13. All contact systems show an increase in wear coefficient with increasing work of adhesion (i.e., decreasing lubrication efficacy). The ceramic–ceramic and metal–metal contact systems exhibit similar wear coefficients; however, they are much higher than those of the ceramic–metallic contact system at any environment. This difference may be attributed to the much lower work of adhesion of the ceramic–metallic contact system, mainly attributed to the very

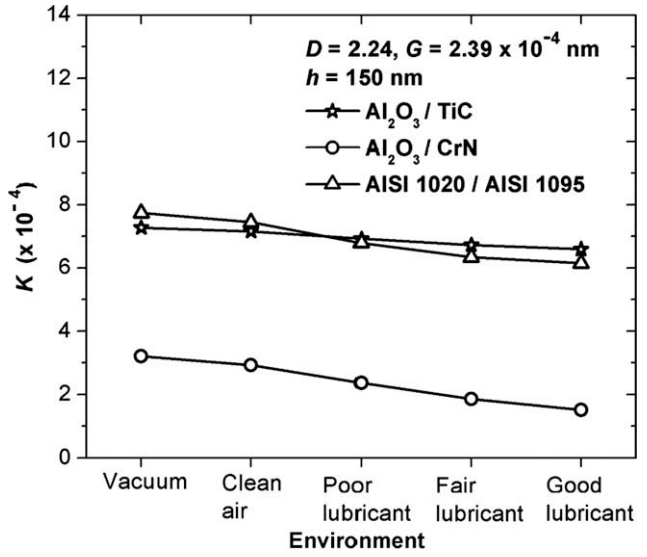

Fig. 13. Wear coefficient K versus environment (interfacial adhesion) for surface properties given in Tables 1 and 2 ($\sigma = 290$ nm).

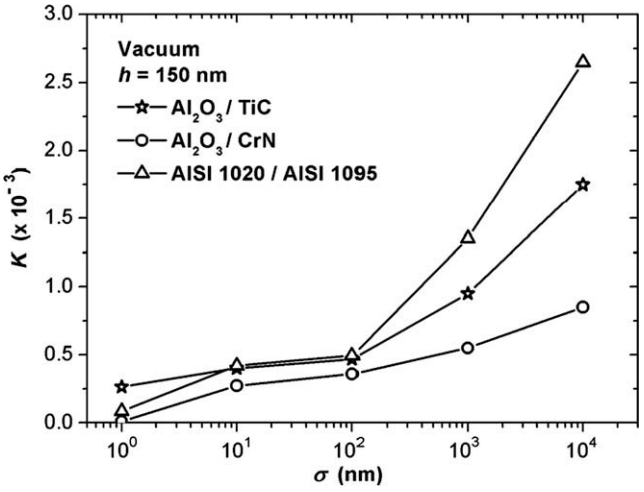

Fig. 14. Wear coefficient K versus rms roughness of equivalent surface σ ($D = 2.24$) for surface properties given in Tables 1 and 2.

low surface energy of the CrN surface (Table 1).

Fig. 14 shows the variation of the wear coefficient K with the rms roughness of the equivalent surface σ for fixed global interference (h = 150 nm) and environment (vacuum). The results reveal the existence of two wear regimes. In the low-roughness regime ($\sigma < 100$ nm), the wear coefficient increases gradually with the surface roughness, assuming values on the order of 10^{-4}, which are in the middle range of adhesive wear coefficient (Rabinowicz, 1995). However, in the high-roughness regime ($\sigma > 100$ nm), the wear coefficient increases more rapidly with the surface roughness, and for metal–metal and ceramic–ceramic interfaces with $\sigma > 1000$ nm it reaches values on the order of 10^{-3} that are usually associated with severe adhesive wear of clean surfaces (Rabinowicz, 1995). The lowest wear coefficient of the ceramic–metallic contact system throughout the examined roughness range is indicative of its superior antiwear characteristics. The trend for the wear coefficient to increase with surface roughness follows the trend shown in Fig. 6. Despite the decrease of a'_{Lk} and a'_{Li} with the roughness increase (or increase in G since $D = 2.24$), the wear coefficient is mostly affected by the magnitude of a'_C (Eqs. (26)–(29)).

4.4. Applicability and extension of the present analysis

In the present analysis, the Hertzian equation of the normal load at a single elastic asperity was modified to include the effect of adhesion (Eq. (10)) following the JKR adhesion model (Johnson et al., 1971). However, the analysis is not restricted to a particular adhesion model. For example, the effect of adhesion on the normal load at a single asperity can also be represented by the DMT adhesion model (Derjaguin et al., 1975) without additional modification of the analysis. The applicability of the JKR or DMT adhesion models can be determined by a dimensionless parameter, referred to as the Tabor parameter (Tabor, 1977), given by

$$\mu = \left(\frac{RW_{AB}^2}{E^{*2}z_0^3}\right)^{1/3} \tag{31}$$

where z_0 is the equilibrium separation distance of the two surfaces. Johnson and Greenwood (1997) have argued that the DMT and JKR models are applicable when $\mu < 0.1$ and $\mu > 5$, respectively.

For the contact systems examined in this study, z_0 was determined based on the method proposed by Yu and Polycarpou (2004), and $c_m c_l$ values corresponding to good lubrication conditions (Table 2) were used to obtain the lowest W_{AB} values for each contact system. Since $R \propto a'$, the smallest truncated area for elastic deformation, i.e., a'_C (Figs. 5 and 6), was used to calculate the asperity radius of curvature in each case. Substituting the values of z_0, W_{AB}, R, and E^* obtained for each contact system into Eq. (31), the Tabor parameter of the ceramic–ceramic, ceramic–metallic, and metal–metal contact systems was found equal to 6.77, 6.21, and 11.2, respectively. These values represent lower bounds of the Tabor parameter because the lowest values of W_{AB} and R of each contact system were used to calculate μ. Because $\mu > 5$ for all interfacial adhesion (lubrication) conditions and the entire range of elastic asperity radius considered in the analysis, it is concluded that the JKR model is suitable for analyzing these contact systems. The present analysis can also be applied to surfaces exhibiting $\mu < 0.1$, provided the contact load equation (Eq. (10)) is replaced by that of the DMT adhesion model.

5. Conclusions

A contact mechanics analysis of adhesive wear of rough (fractal) surfaces was performed to elucidate the dependence of plastic deformation at asperity contacts and wear rate (coefficient) on global interference (normal load), elastic–plastic material properties, topography (roughness), and work of adhesion of the contacting surfaces. Material loss (wear) was presumed to originate from fully-plastic asperity contacts, accounting for the contribution of interfacial adhesion to the normal load at each asperity contact. Numerical results for representative contact systems revealed the effects of material properties, roughness, surface compatibility, and environmental conditions on the adhesive wear rate and wear coefficient. Based on the presented results and discussion, the following main conclusions can be drawn from this study.

1. Plastic deformation at asperity contacts is controlled by the critical truncated contact area, which depends on the elastic–plastic material properties, topography (roughness), and work of adhesion (affected by the material compatibility and contact environment or lubrication condition) of the contacting surfaces.
2. The number of plastically deformed asperity contacts increases rapidly with the global interference. However, the plastic truncated contact area is much less (<1–2%) than the total truncated contact area, revealing the dominance of elastic deformation at the asperity level over a wide range of global interference.
3. The wear rate increases monotonically with the global interference, whereas the wear coefficient decreases rapidly to a steady state, showing a weak dependence on normal load.
4. Both the wear rate and the wear coefficient decrease with the work of adhesion (interfacial adhesion) and increase with the roughness of the contacting surfaces.
5. The adhesive wear coefficient may vary significantly (in the range of $\sim 10^{-4}$–10^{-3} for the contact systems examined), depending on the material properties, surface topography (roughness), and work of adhesion that depends on the surface energies of the contacting surfaces and interfacial adhesion controlled by the material compatibility and contact environment.

Acknowledgment

This research was partially funded by Intel Co. under Grant No. 78550.

References

Archard, J.F., 1953. Contact and rubbing of flat surfaces. Journal of Applied Physics 24, 981–988.

Bhushan, B., Israelachvili, J.N., Landman, U., 1995. Nanotribology: friction, wear and lubrication at the atomic scale. Nature 374, 607–616.
Borri-Brunetto, M., Carpinteri, A., Chiaia, B., 1999. Scaling phenomena due to fractal contact in concrete and rock fractures. International Journal of Fracture 95, 221–238.
Ciavarella, M., Demelio, G., Barber, J.R., Jang, Y.H., 2000. Linear elastic contact of the Weierstrass profile. Proceedings of the Royal Society of London Series A 456, 387–405.
Derjaguin, B.V., Muller, V.M., Toporov, Y.P., 1975. Effect of contact deformations on the adhesion of particles. Journal of Colloid and Interface Science 53, 314–326.
Finkin, E.F., 1972. Speculations on the theory of adhesive wear. Wear 21, 103–114.
Gong, Z.-Q., Komvopoulos, K., 2005a. Thermomechanical analysis of semi-infinite solid in sliding contact with a fractal surface. Journal of Tribology 127, 331–342.
Gong, Z.-Q., Komvopoulos, K., 2005b. Contact fatigue analysis of an elastic–plastic layered medium with a surface crack in sliding contact with a fractal surface. Journal of Tribology 127, 503–512.
Greenwood, J.A., Williamson, J.B.P., 1966. Contact of nominally flat surfaces. Proceedings of the Royal Society of London Series A 295, 300–319.
Johnson, K.L., Greenwood, J.A., 1997. An adhesion map for the contact of elastic spheres. Journal of Colloid and Interface Science 192, 326–333.
Johnson, K.L., Kendall, K., Roberts, A.D., 1971. Surface energy and the contact of elastic solids. Proceedings of the Royal Society of London Series A 324, 301–313.
Kogut, L., Etsion, I., 2002. Elastic–plastic contact analysis of a sphere and a rigid flat. Journal of Applied Mechanics 69, 657–662.
Kogut, L., Komvopoulos, K., 2004. Analysis of the spherical indentation cycle for elastic–perfectly plastic solids. Journal of Materials Research 19, 3641–3653.
Komvopoulos, K., 2008. Effects of multi-scale roughness and frictional heating on solid body contact deformation. Comptes Rendus Mécanique 336, 149–162.
Komvopoulos, K., Gong, Z.-Q., 2007. Stress analysis of a layered elastic solid in contact with a rough surface exhibiting fractal behavior. International Journal of Solids and Structures 44, 2109–2129.
Komvopoulos, K., Yan, W., 1997. A fractal analysis of stiction in microelectromechanical systems. Journal of Tribology 119, 391–400.
Komvopoulos, K., Yan, W., 1998. Three-dimensional elastic–plastic fractal analysis of surface adhesion in microelectromechanical systems. Journal of Tribology 120, 808–813.
Komvopoulos, K., Yang, J., 2006. Dynamic analysis of single and cyclic indentation of an elastic–plastic multi-layered medium by a rigid fractal surface. Journal of the Mechanics and Physics of Solids 54, 927–950.
Komvopoulos, K., Ye, N., 2001. Three-dimensional contact analysis of elastic–plastic layered media with fractal surface topographies. Journal of Tribology 123, 632–640.
Komvopoulos, K., Zhang, H.-S., 2008. Elastic modulus and hardness data extracted from nanoindentation measurements (unpublished).
Kruschov, M.M., 1957. Resistance of metals to wear by abrasion, as related to hardness. In: Proceedings of Conference on Lubrication and Wear, Institution of Mechanical Engineers, London, pp. 655–659.
Lisowski, Z., Stolarski, T.A., 1981. A modified theory of adhesive wear in lubricated contacts. Wear 68, 333–345.
Majumdar, A., Bhushan, B., 1990. Role of fractal geometry in roughness characterization and contact mechanics of surfaces. Journal of Tribology 112, 205–216.
Majumdar, A., Bhushan, B., 1991. Fractal model of elastic–plastic contact between rough surfaces. Journal of Tribology 113, l–11.
Mandelbrot, B.B., 1975. Stochastic models for the Earth's relief, the shape and the fractal dimension of the coastlines, and the number-area rule for islands. Proceedings of the National Academy of Sciences of the United States of America 72, 3825–3828.
Mandelbrot, B.B., 1983. The Fractal Geometry of Nature. Freeman, New York. pp. 1–83 and 116–118.
Martin, C.J., Mikkelson, A.R., Tejeda, R.O., Engelstad, R.L., Lovell, E.G., Blaedel, K.L., Claudet, A.A., 2002. Mechanical modeling of the reticle and chuck for EUV lithography. In: Engelstad, R.L. (Ed.), Emerging Lithographic Technologies VI, Proceedings of SPIE, vol. 4688, pp. 194–204.
Mukherjee, S., Ali, S.M., Sahoo, P., 2004. An improved elastic–plastic contact model of rough surfaces in the presence of adhesion. Proceedings of the Institution of Mechanical Engineers, Part J: Journal of Engineering Tribology 218, 557–567.
Nayak, P.R., 1973. Random process model of rough surfaces in plastic contact. Wear 26, 305–333.
Paretkar, R.K., Modak, J.P., Ramarao, A.V., 1996. An approximate generalized experimental model for dry sliding adhesive wear of some single-phase copper-base alloys. Wear 197, 17–37.
Persson, B.N.J., Bucher, F., Chiaia, B., 2002. Elastic contact between randomly rough surfaces: comparison of theory with numerical results. Physical Review B 65, 184106-1–184106-7.
Qureshi, F.S., Sheikh, A.K., 1997. A probabilistic characterization of adhesive wear in metals. IEEE Transactions on Reliability 46, 38–44.
Rabinowicz, E., 1977. Friction, Wear and Lubrication: A Self-Study Subject, second ed. MIT Press, Cambridge, MA. pp. 2.8–2.13 and 3.1–3.9.
Rabinowicz, E., 1980. An adhesive wear model based on variations in strength values. Wear 63, 175–181.
Rabinowicz, E., 1995. Friction and Wear of Materials, second ed. Wiley, New York. pp. 143–190.
Roy Chowdhury, S.K., Pollock, H.M., 1981. Adhesion between metal surfaces: the effect of surface roughness. Wear 66, 307–321.
Sahoo, P., 2006. Adhesive friction for elastic–plastic contacting rough surfaces considering asperity interaction. Journal of Physics D: Applied Physics 39, 2809–2818.
Sahoo, P., Banerjee, A., 2005. Asperity interaction in elastic–plastic contact of rough surfaces in presence of adhesion. Journal of Physics D: Applied Physics 38, 2841–2847.
Sahoo, P., Roy Chowdhury, S.K., 1996. A fractal analysis of adhesion at the contact between rough solids. Proceedings of the Institution of Mechanical Engineers, Part J: Journal of Engineering Tribology 210, 269–279.
Sahoo, P., Roy Chowdhury, S.K., 2002. A fractal analysis of adhesive wear at the contact between rough solids. Wear 253, 924–934.
Shirong, G., Gouan, C., 1999. Fractal prediction models of sliding wear during the running-in process. Wear 231, 249–255.
Suh, N.P., 1973. The delamination theory of wear. Wear 25, 111–124.
Suh, N.P., 1986. Tribophysics. Prentice-Hall, Englewood Cliffs, NJ. p. 66.
Tabor, D., 1977. Surface forces and surface interactions. Journal of Colloid and Interface Science 58, 2–13.
Wang, S., Komvopoulos, K., 1994a. A fractal theory of the interfacial temperature distribution in the slow sliding regime: Part I – elastic contact and heat transfer analysis. Journal of Tribology 116, 812–823.
Wang, S., Komvopoulos, K., 1994b. A fractal theory of the interfacial temperature distribution in the slow sliding regime: Part II – multiple domains, elastoplastic contacts and applications. Journal of Tribology 116, 824–832.
Wang, S., Komvopoulos, K., 1995. A fractal theory of the temperature distribution at elastic contacts of fast sliding surfaces. Journal of Tribology 117, 203–215.
Warren, C.D., Wert, J.J., 1990. A model for adhesive wear. Journal of Adhesion Science and Technology 4, 177–196.
Yan, W., Komvopoulos, K., 1998. Contact analysis of elastic–plastic fractal surfaces. Journal of Applied Physics 84, 3617–3624.
Yang, L.J., 2003. An integrated transient and steady-state adhesive wear model. Tribology Transactions 46, 369–375.
Yang, L.J., 2004. Prediction of steady-state wear coefficients in adhesive wear. Tribology Transactions 47, 335–340.
Yang, J., Komvopoulos, K., 2005. A mechanics approach to static friction of elastic–plastic fractal surfaces. Journal of Tribology 127, 315–324.
Yu, N., Polycarpou, A.A., 2004. Adhesive contact based on the Lennard-Jones potential: a correction to the value of the equilibrium distance as used in the potential. Journal of Colloid and Interface Science 278, 428–435.
Zhou, G.Y., Leu, M.C., Blackmore, D., 1993. Fractal geometry model for wear prediction. Wear 170, l–14.